

A study of two FRBs with low polarization fractions localized with the MeerTRAP transient buffer system

K. M. Rajwade^{1,2}★ L. N. Driessen³★† E. D. Barr⁴ I. Pastor-Marazuela⁵ M. Berezina,^{4,6} F. Jankowski^{5,7} A. Muller,⁸ L. Kahinga,⁹ B. W. Stappers,⁵ M. C. Bezuidenhout^{10,11} M. Caleb^{10,3}, A. Deller¹² W. Fong,¹³ A. Gordon^{10,13} M. Kramer⁴ M. Malenta,⁵ V. Morello^{10,14} J. X. Prochaska,⁹ S. Sanidas,⁵ M. Surnis¹⁵ N. Tejos^{10,16} and S. Wagner⁶

¹*Astrophysics, University of Oxford, Denys Wilkinson Building, Keble Road, Oxford OX1 3RH, UK*

²*ASTRON, 4 Oude Hoogeveensedijk, Dwingeloo 7991 PD, The Netherlands*

³*Sydney Institute for Astrophysics, School of Physics, University of Sydney, NSW, Sydney 2006, Australia*

⁴*Max-Planck-Institut für Radioastronomie, Auf dem Hügel 69, D-53121 Bonn, Germany*

⁵*Jodrell Bank Centre for Astrophysics, University of Manchester, Oxford Road, Manchester M13 9PL*

⁶*Landessternwarte, Universität Heidelberg, Königstuhl 12, D-69117 Heidelberg, Germany*

⁷*LPC2E, Université d'Orléans, CNRS, 3A Avenue de la Recherche Scientifique, F-45071 Orléans, France*

⁸*Maria Mitchell Observatory, Nantucket, MA 02554, USA*

⁹*University of California, Santa Cruz, 1156 High Str, Santa Cruz, CA 95064, USA*

¹⁰*Department of Mathematical Sciences, University of South Africa, Cnr Christiaan de Wet Rd and Pioneer Avenue, Florida Park, 1709, Roodepoort, South Africa*

¹¹*Centre for Space Research, North-West University, Potchefstroom 2531, South Africa*

¹²*Centre for Astrophysics and Supercomputing, Swinburne University of Technology, Hawthorn, VIC 3122, Australia*

¹³*Center for Interdisciplinary Exploration and Research in Astrophysics (CIERA), Department of Physics and Astronomy, Northwestern University, Evanston, IL 60208, USA*

¹⁴*SKA Observatory, Jodrell Bank, Lower Withington, Macclesfield SK119FT, UK*

¹⁵*Department of Physics, IISER Bhopal, Bhauri Bypass Road, Bhopal 462066, India*

¹⁶*Instituto de Física, Pontificia Universidad Católica de Valparaíso, Casilla 4059, Valparaíso, Chile*

Accepted 2024 July 2. Received 2024 July 1; in original form 2024 May 8

ABSTRACT

Localization of fast radio bursts (FRBs) to arcsecond and subarcsecond precision maximizes their potential as cosmological probes. To that end, FRB detection instruments are deploying triggered complex-voltage capture systems to localize FRBs, identify their host galaxy, and measure a redshift. Here, we report the discovery and localization of two FRBs (20220717A and 20220905A) that were captured by the transient buffer system deployed by the MeerTRAP instrument at the MeerKAT telescope in South Africa. We were able to localize the FRBs to precision of ~ 1 arcsecond that allowed us to unambiguously identify the host galaxy for FRB 20220717A (posterior probability ~ 0.97). FRB 20220905A lies in a crowded region of the sky with a tentative identification of a host galaxy but the faintness and the difficulty in obtaining an optical spectrum preclude a conclusive association. The bursts show low linear polarization fractions (10–17 per cent) that conform to the large diversity in the polarization fraction observed in apparently non-repeating FRBs akin to single pulses from neutron stars. We also show that the host galaxy of FRB 20220717A contributes roughly 15 per cent of the total dispersion measure (DM), indicating that it is located in a plasma-rich part of the host galaxy which can explain the large rotation measure. The scattering in FRB 20220717A can be mostly attributed to the host galaxy and the intervening medium and is consistent with what is seen in the wider FRB population.

Key words: techniques: interferometric – stars: neutron – radio continuum: transients.

1 INTRODUCTION

Fast radio bursts (FRBs) are intense, millisecond-duration radio flashes that originate from cosmological distances (Lorimer et al.

2007). They have remained one of the most enigmatic astrophysical mysteries since their discovery over a decade ago. Several theories have been proposed to explain their origin but we still lack any definitive evidence to decipher their nature. The detection of repeating FRBs allowed astronomers to regularly monitor the sources and enable precise localization to their host galaxies (Tendulkar et al. 2017). These follow-up studies have been important to put constraints on their progenitors. The discovery of FRB-like bursts

* E-mail: kaustubh.rajwade@physics.ox.ac.uk (KR); laura.driessen@sydney.edu.au (LD)

† Both authors contributed equally.

from a Galactic magnetar SGR J1935 + 2154 suggests that highly magnetized neutron stars (magnetars) have the ability to produce luminous radio bursts (Bochenek et al. 2020; CHIME/FRB Collaboration et al. 2020). This suggested that we should expect FRBs in star-forming regions of their host galaxies where most of the magnetars are produced via core-collapse supernovae. This conjecture was put to the test again when a repeating FRB was discovered and localized to a globular cluster in a near-by galaxy M81 (Kirsten et al. 2022). One needs to invoke exotic models for the creation of magnetars in an environment that is dominated by an old stellar population. These results already show the importance of precise localizations of FRBs and their environs that provide important clues about their progenitors. Moreover, it also could help in determining the distribution of FRBs across different galaxy types, probe the intergalactic medium with extreme precision and count the ‘missing’ baryons and their distribution (Macquart et al. 2020). All of these advancements can lead to a deeper understanding of the physics behind these enigmatic signals.

Until a few years ago, precise localization of the FRBs was only possible with repeating FRBs as it allows for regular follow-up using radio interferometers. However, recent advancements in instrumentation and observing strategies have enabled arc-second localizations of one-off FRBs, opening up the field entirely. The most significant breakthrough in localizing single FRBs came with the development of the commensal real-time ASKAP FAST Transients survey (CRAFT; Bannister 2018). CRAFT enabled ASKAP to detect and localize FRBs in real-time, providing rapid follow-up optical observations and identification of host galaxies. Since then, other radio telescopes have followed suit and are now spear-heading the real-time localization efforts of one-off FRBs (Bannister 2018; CHIME/FRB Collaboration et al. 2018; Ravi et al. 2023). In this paper, we report two subarcsecond localizations of FRBs using the transient buffer capture mode on MeerTRAP: a commensal, real-time FRB detector at the MeerKAT telescope in South Africa. The paper is organized as follows. In Section 2, we describe the transient buffer capture system. In Section 3, we describe the discovery, localization and optical follow-up of the first two FRBs with this system. In Section 4, we discuss the properties of the FRBs and their host galaxies and in Section 5, we summarize our results and conclusions.

2 MEERTRAP TRANSIENT BUFFER SYSTEM

2.1 The real-time search

The detailed description of the real-time FRB detection system has been presented in Rajwade et al. (2020) and Rajwade et al. (2022). Fig. 1 shows the detailed flow diagram of the system. Raw data from each antenna are channelized using a poly-phase filter (van der Byl et al. 2022) to create a discretely channelized complex voltage datastream. This datastream is acquired by the Filterbank BeamFormer User Supplied Equipment (FBFUSE), where these data are detected and converted into total power beams across the FoV of MeerKAT. MeerTRAP observations typically use only the inner 40 dishes of the MeerKAT array for beamforming. This is a trade-off between sensitivity and achievable field of view (FoV) given the finite compute resources available to FBFUSE (Chen et al. 2021). Even when only beamforming a subset of the antennas, FBFUSE ingests the full complement of channelized voltages from the MeerKAT antennas. This is essential for the operation of the transient buffer. The Transient User Supplied Equipment (TUSE) receives the coherent total power beams from FBFUSE and runs a real-time search on the data for FRBs and other transients.

2.2 Detection and trigger

In order to save complex voltages from the telescope, it is important to send out prompt triggers to the beamformer immediately after the detection of an FRB to initiate data extraction. Typically, the real-time system has to process the data, classify the candidates, and send a trigger within 45 s of receiving the data from the beamformer. To that end, we decided to use low-latency VOEvent alerts to communicate triggers. That is because VOEvents are well established in the transient community, a software ecosystem exists, a VOEvent standard for FRB alerts had already been proposed (Petroff et al. 2017), and was subsequently adopted at several radio telescopes, most notably CHIME. For MeerTRAP, we implemented a VOEvent-based software to trigger the voltage buffer read-out on the FBFUSE cluster from the real-time transient detection system running on the TUSE servers (Jankowski et al. 2022). VOEvent messages are in XML format (Seaman et al. 2011) and contain the parameters of the alert, e.g. a unique identifier, the author, the event time, its sky position, and the instrumental set-up. The event packets are distributed by brokers, for which we employ the COMET software (Swinbank 2014), both locally on the MeerTRAP head nodes and the central MeerKAT observatory-wide broker. A containerized COMET subscriber runs on the FBFUSE head node, waiting for events. When an FRB, or any other transient, is detected by the MeerTRAP pipeline, its parameters are written into a VOEvent message which is sent to the local COMET broker and forwarded to the observatory-wide one. The alert is then received by the FBFUSE subscriber which parses the contents and converts them into a request to write-out the corresponding complex voltage data from the transient buffer. More details are presented in Jankowski et al. (2022) and software are available online.¹ Using VOEvents has the advantage that we can easily disseminate our triggers to external collaborators in the future.

2.3 Extraction of complex voltage data and phase-up

Data from MeerKAT channelizers arrive on the FBFUSE cluster as a 1.8 Tb/s Ethernet stream, split over 256 multicast groups, with each group containing 1/256th of the full MeerKAT bandwidth for all the available antennas included in the current observations. The groups are split such that each of the 32-servers that comprise the FBFUSE cluster ingests 8 groups, 4 per network interface. Physically, the processing for each set of 4 multicast groups is mapped to a single non-uniform memory architecture (NUMA) node, hosting a network card, CPU, GPU and 192 GB of DDR4 RAM. The depth of the transient buffer that can be accommodated on such a system is determined by $t_{\text{tb}} = 8M/(2N_{\text{pol}}N_{\text{ant}}BN_{\text{bits}})$ s, where M is the available memory in bytes, N_{pol} is the number of polarizations, N_{ant} is the number of antennas being ingested, B is the received bandwidth per NUMA node in Hz and N_{b} is the bit depth per sample. For MeerKAT, we have $N_{\text{pol}} = 2$, $N_{\text{bits}} = 8$, $N_{\text{ant}} \leq 64$ and $B = 8.5$, 13.375, or 13.671875 MHz at UHF (816 MHz), L band (1.4 GHz), and S band (2.2 GHz), respectively. Approximately, 95 per cent of the RAM (~ 182 GB) on each FBFUSE NUMA node is available for the transient buffer; hence, we achieve a buffer depth of ~ 54 , 56, and 88 s at L band (1284 MHz), UHF (816 MHz), and S band (2500 MHz) for the full array. The buffer depth may be increased by moving to a lower bandwidth receiver or by specifying that only a subset of the current subarray be used (although it should be noted that the subset used by the transient buffer defines the superset available

¹<https://github.com/fjankowsk/meertrig/>

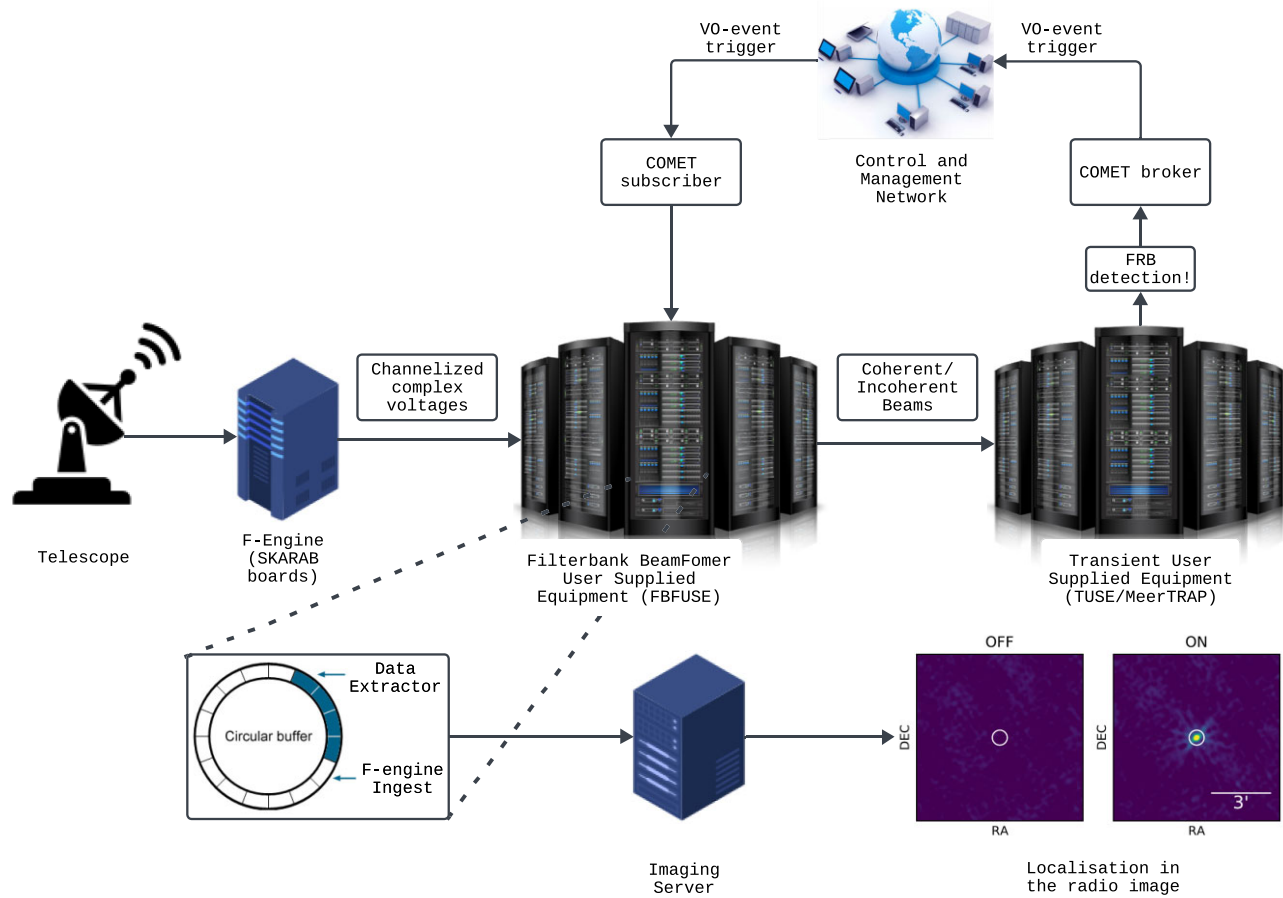


Figure 1. A flow chart showing the entire transient buffer trigger pipeline (see the text for details). Here, the F-engine corresponds to where the poly-phase filter is applied on the complex voltages streaming from the telescope. The figure has been created using LUCID CHART.

for beamforming). Depending on the number of frequency channels requested from the MeerKAT correlator, the time resolution of the transient buffer data varies from 1.9 to 36 μ s.

As illustrated in Fig. 2, the FBFUSE transient buffer is implemented as a PSRDADA² shared memory ring buffer (SMRB) with one writer and two readers. The writing process captures data from the MeerKAT correlator network, orders it by time, antenna and frequency and writes it to the SMRB. The primary reading process is the beamformer itself, which operates in real time, consuming and processing blocks from the SMRB as they become available. The secondary reading process is the transient buffer data extractor. This process does not immediately read blocks from the SMRB but instead monitors the overall usage of the SMRB and holds open blocks in the buffer, only releasing them when the overall occupancy of the buffer reaches 95 per cent. It thus guarantees that at least 95 per cent of the buffer is maintained in memory at all times. The remaining 5 per cent of the buffer is required to be left unoccupied to allow sufficient time for data extraction and processing on receipt of a trigger event (see below) such that the writing process is not blocked, resulting in data loss.

The triggers received by FBFUSE are propagated to the buffer data extractor process via a UNIX socket. Each is formatted as a JSON message containing a DM, reference frequency, start UTC,

end UTC, and trigger identifier. The start and end UTC along with the reference frequency and DM define the section of data to be extracted from the transient buffer. As noted above, extraction of data from the SMRB must be sufficiently fast as to avoid blocking the writing process. Several tests have shown that the instrument can safely write up to 300 ms of the buffer to disc at a time without affecting the capture of data from the MeerKAT correlator network. As 300 ms may be shorter than duration of the time delay of a highly dispersed FRB, the buffer data extractor incoherently dedisperses the buffer data at the time of extraction. Upon receipt of a trigger, the buffer data extractor re-references the start and end UTCs of the trigger to the highest frequency in the currently processed subband and scans through the buffer until it reaches the block containing the start of the event. The frequency channels and times corresponding to the event window are then extracted for all antennas and polarizations and written to a temporary memory buffer in dedispersed order. This process continues over subsequent blocks until the end of the event is reached, at which point the temporary memory buffer is written to disc with a header containing observation and trigger metadata. This process is illustrated in the right-hand panel of Fig. 2.

In order to aide in the downstream analysis of the extracted voltages, FBFUSE records a snapshot of the current complex gain solutions as calculated by the MeerKAT Science Data Processor (Jonas & MeerKAT Team 2016). These are written locally as NUMPY arrays to be applied to the transient buffer data extracted for any FRB.

²<https://psrdada.sourceforge.net/>

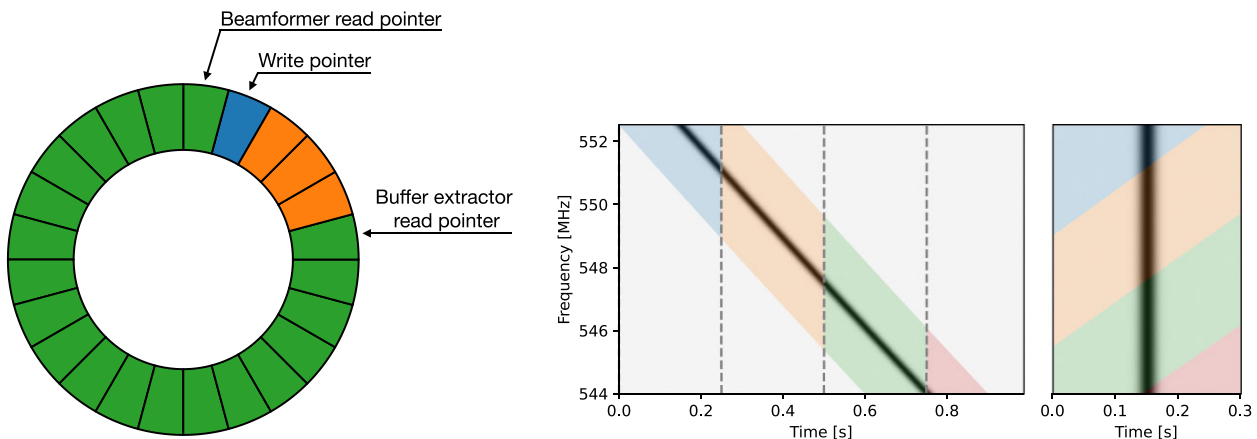


Figure 2. Left: Shared memory ring buffer configuration for the FBFUSE transient buffer. Each segment represents a block of memory in the ring buffer, with blue showing a block that is being written to, green showing blocks that are occupied and orange showing blocks that free and can be written to. Shown are the positions of the write pointer for data coming from the MeerKAT correlator network, the beamformer read pointer for data going through the FBFUSE beamforming pipeline and the buffer extractor read pointer for data being recorded upon receipt of a trigger. The write pointer progresses through the buffer in a clock-wise direction. Right: The algorithm that extracts the data corresponding to the DM of the detected FRB after accounting for the dispersion delay. The dispersion delay has been shown here as a linear trend for simplicity. The FRB data are spread across several data blocks due to the delay as shown by the dashed vertical lines. The coloured regions show the data that are extracted from each data block.

2.4 Imaging and localization

2.4.1 Producing measurement sets

The extracted transient buffer data are correlated using xGPU³ (Clark, La Plante & Greenhill 2011). These data already have the geometric delays applied and we apply the gain and phase solutions to each antenna, time and frequency channel to phase-up the data to the pointing centre of the observation using the solutions obtained during the initial delay calibration. Each file produced contains one subband (1/64th of the full bandwidth) and, due to dispersion correction, has a different start time. In order to calibrate and image the correlated visibilities, they need to be packaged with appropriate metadata (e.g. phase centre position, baseline direction cosines, etc.) in a recognized visibility file format such as FITS-Interferometry Data Interchange (IDI) format⁴ or a Measurement Set (MS). We made use of the DIFX2FITS application provided by DIFX (Deller et al. 2007, 2011) to produce FITS-IDI files that could subsequently be converted to an MS using CASA (McMullin et al. 2007), after providing the necessary metadata in the format expected by the DIFX2FITS application.

First we use SCHED,⁵ a program often used to schedule Very Long Baseline Interferometry (VLBI) observations. Although scheduling is not necessary, the software produces the output files describing the details of the MeerKAT observation in a format that DIFX can read. Hence, we first generate several files required to run SCHED. This includes the station file with the location of the MeerKAT antennas that were used, a frequency file with the frequency set-up, and the main KEY file with instructions for Sched. At this stage, we also generate the V2D file with information on the observing set-up, Earth orientation and antenna clock offsets that will be used by DIFX. Once

these files are created, we run Sched, which produces the VEX files that will be the input for DIFX.

We then run the DIFX functions vex2difx and calcif2 to produce a model of the geometric delays. We now have the delay model and *uvw*-plane values required to assign to the xGPU correlated visibilities. We next re-structure the xGPU visibilities into a DIFX format, including the metadata required such as the polarization, band, and baseline. Finally, we use the DIFX function difx2fits to convert the file into a FitsFile.

For every different number of baselines a new version of xGPU needs to be compiled. We would ideally always be observing with and saving data from all 64 MeerKAT dishes; however, this is not always the case. To avoid compiling multiple versions of xGPU, we assume that we always have 64 dishes. To do this, we create fake antenna files prior to the xGPU step that we can later flag. For example, if we have only 60 dishes in an observations we create 4 copy antennas to pad to 64 dishes. Now that we have a DIFX fits file, we read this in to CASA using importfitsidi. We then use CASA (The CASA Team et al. 2022) to flag the copied/fake antennas and the autocorrelations. Finally, we output the data as an MS that we can image.

2.4.2 Producing images and transient localization

We now have one MS for each of the 64 frequency subbands. Since each MS technically has a different start time, instead of performing a joint deconvolution on all of the MSs together, we image each MS individually. We first perform a simple, dirty clean on each MS using wsclean, and visually inspect the resulting images. This allows us to manually exclude channels dominated by RFI. This process will be automated in the future. We exclude those parts of the band that are dominated by RFI by excluding those MSs. We then produce a frequency and time average image by adding each dirty image together and dividing by the number of images. We compare this frequency and time averaged image to e.g. the ASKAP RACS-Mid

³xGPU: <https://github.com/GPU-correlators/xGPU>

⁴<https://lweb.cfa.harvard.edu/~jzhao/SMA-FITS-CASA/docs/AIPSMEMO102.pdf>

⁵Sched: <http://www.aoc.nrao.edu/software/sched/>

(Duchesne et al. 2023) of the same area of the sky to confirm that our image reflects reality.

In order to detect an FRB, we need to re-image each MS to produce images with shorter integration times. We expect the FRB to be close to the centre of the 300 ms due to the DM-slicing process, and therefore, we image in an odd number of time bins. We image in 11 time bins and proceed to average each time bin in frequency by adding the images in each bin together and dividing by the number of images. We now have one frequency averaged image per time bin.

Each transient buffer data set is 300 ms long, which means that the *uv*-plane does not rotate significantly over the observation, and we do not expect the noise to change substantially over the data set, even when taking into account the dispersion delay. This means that we can perform difference imaging to find the FRB. We do this by subtracting our time and frequency-averaged image from each frequency-averaged time bin image. We then visually inspect the resulting difference images to find the FRB. If we find the burst we confirm that it is the FRB by checking that it appears in the image corresponding to the FRB arrival time.

Next, we produce images with shorter integration times around the time bins where the FRB was seen, so that we can accurately select all the time bins where it was detected. We integrate these time bins to produce an ‘on’ image, and then produce an ‘off’ image with the same integration time where the FRB was not visible. We produce these images with more advanced cleaning parameters in `WSClean`, which we also apply to the full integration time image. The `WSClean` parameters we use for the stopping criteria are 100 iterations, or a threshold of 0.01 (arbitrary units). We apply a Cotton-Schwab cleaning with major iteration gain of 0.8, and automasking with $\sigma = 3$. We apply a Briggs weighting with a robustness parameter of -0.3 , and a weighting rank filter of 3. Finally, we use W-gridding on the data.

2.5 Astrometry

We corrected the absolute astrometry of the radio sources in the FoV of the detected FRBs using the method described in Driessen et al. (2022) and Driessen et al. (2024). We used the Python Blob Detector and Source Finder⁶ (PYBDSF) to determine the positions of sources in the full integration time, ‘on’ and ‘off’ images, which we used to determine and correct the accuracy of our absolute astrometry.

For the astrometric corrections, where possible, we prioritized using reference catalogues that use VLBI to achieve milliarcsecond precision on the position, such as the Long Baseline Array (LBA) Calibrator Survey (LCS1; Petrov et al. 2011). Alternatively, the Australian Telescope Compact Array (ATCA) Parkes-MIT-NRAO (PMN) (ATPMN; McConnell et al. 2012) has an astrometric accuracy of 0.4 arcsec in RA and Dec. However, these catalogues do not always have sufficient sources in the FoV of the images where the FRBs were localized. The Rapid ASKAP Continuum Survey (RACS; Hale et al. 2021), on the other hand, usually contains tens to hundreds of sources within the FoV, but the astrometric accuracy of the source positions has systematic offsets of $\sim 1\text{--}2$ arcsec due to the lack of sufficient radio sources with VLBI positions in the Southern Hemisphere to perform accurate astrometric corrections of the catalogue.

The Radio Fundamental Catalog (RFC⁷), which provides positions with milliarcsecond accuracy, often contains more sources in the FoV of interest than LCS1 or ATPMN, but not enough to use on its own.

When that was the case, we used RFC sources in a larger FoV than the image to correct the positions of the RACS sources, and finally used these corrected RACS positions to align the coordinates of the sources in the full integration MeerKAT images, using the `astroalign` module (Beroiz, Cabral & Sanchez 2020) in PYTHON. We selected unresolved RACS sources with an uncertainty in both RA and Dec <0.5 arcsec and a total flux >20 mJy.

Once we obtained the transformation matrix for the full integration time image, we applied it to the ‘on’ and ‘off’ images and source positions to obtain the corrected FRB coordinates. We computed the average separation between the corrected and reference sources after each alignment, and added them in quadrature to obtain the total astrometric error on the FRB position. The details about the astrometric corrections we performed are given in the Appendix.

2.6 Offline beamforming

Along with offline imaging, the channelized complex voltages saved to disc can be used to form beams at the best-known location of the transient that is determined from the imaging and localization. To do that, the corresponding gain solutions saved by the beamformer are used to phase up the interferometer to the phase centre of the observation. To form a phased beam at the location of the transient, one needs to multiply the gain/phase solutions by appropriate weights. In simple terms, this means adding an extra rotation phase to the existing vector of beamformed weights at the phase centre of the observation. To obtain these additional phase corrections, we use MOSAIC (Chen et al. 2021) to compute the delay polynomials for each antenna i.e. the expected delays that need to be added to each antenna to align the phase of the electric field from a given location in the sky. These are in-turn used to generate the beam weights as function of antenna and frequency. Since we extract the buffer data after compensating for the dispersion delay at each frequency channel, we generate the delay polynomials for each frequency separately based on the slightly different epoch of observation (corresponding to the dispersion delay at that frequency) before computing the weights. We note that these delays are similar to the delays computed during the imaging of these data and the differences are negligible. These weights are finally multiplied with the gain/phase solutions before they are applied to the channelized voltage data from the transient buffer. This process produces a phased up coherent beam at the location of the transient. Forming a coherent beam at the location of the transient has significant advantages: (1) the coherent beam contains all the antennas in the array unlike the core antennas typically used in the real-time search which increases the S/N of the detection (2) the coherent beams overlap at the 25 per cent power point which means that FRBs that fall between two coherent beams get a significant boost (factor of ~ 4) (3) the formed beam has the highest time-resolution possible with the correlator configuration and (4) there is polarization information available in the buffer data which can be used to study the polarization properties of the transient. The scripts used for offline beamforming are provided in an online repo⁸.

Before any scientific utilization of polarization data can be done, it is important to take into account the effects of the primary beam on the polarization properties of the instrument. For a coherent beam that is pointing at a given location x, y (where the origin is at the boresight of the primary beam) within the primary FoV, the measured electric field vector (for an elliptically polarized wave) for the electric field

⁶<https://www.astron.nl/citt/pybdsf/>

⁷RFC: <http://astrogeo.org/rfc/>

⁸<https://gitlab.com/kmrajwade/tbeamformer>

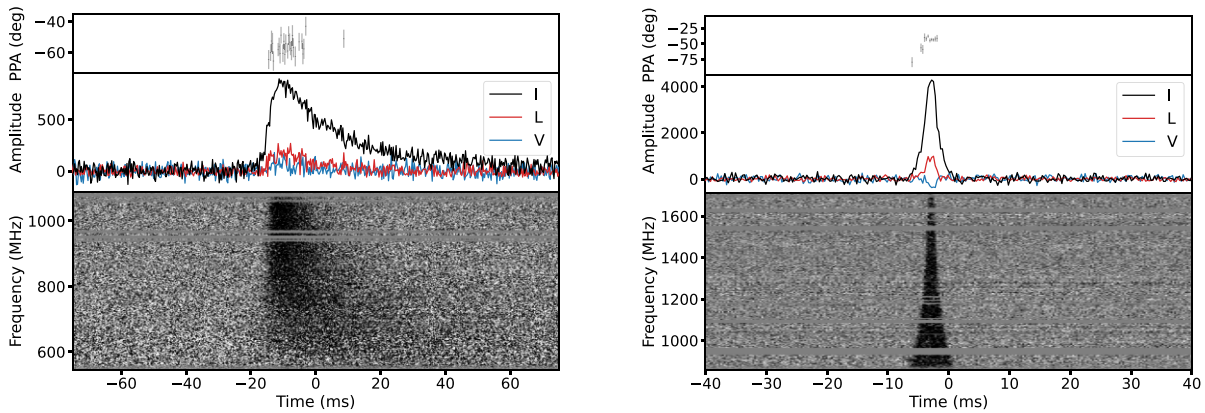


Figure 3. Calibrated polarization emission profiles for FRB 20220717A and FRB 20220905A created from the transient buffer data. The data for FRB 20220717A was dedispersed at the scattering-corrected DM while FRB 20220905A was dedispersed at a DM that accounts for the intra-channel DM smearing at the bottom of the band. The top panels show the absolute polarization position angle and the bottom panels show the total intensity (black), linear polarization (red), and circular polarization (blue).

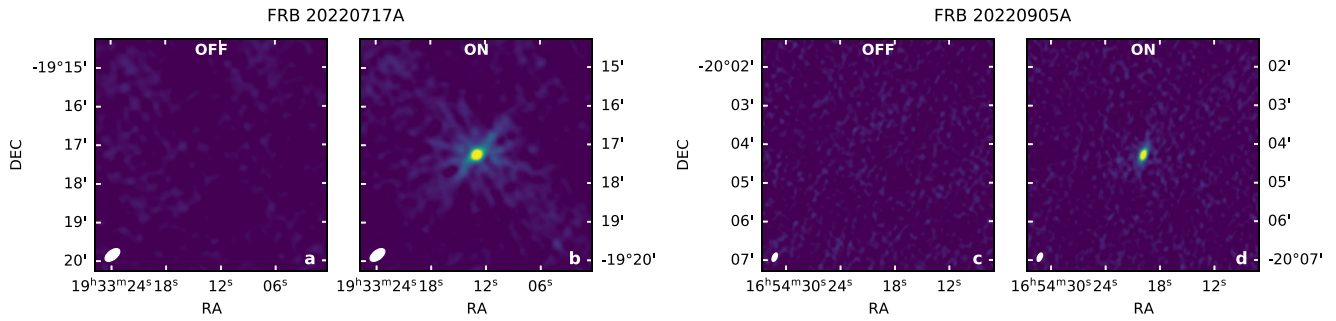


Figure 4. MeerKAT images of the localization of FRB 20220717A and FRB 20220905A. Panel a shows a 43 ms integration of the region before the FRB detection (OFF), while panel b shows a 43 ms integration where the FRB was detected and localized (ON). The synthesized beam is shown on the lower left corner of each image. Panels (c) and (d) show similar images for FRB 20220905A for 7.7 ms integration.

for each hand (H and V) of polarization per antenna, per frequency channel,

$$\epsilon'_{H,V}(x, y, i, v) = \mathcal{J}_{H,V} \epsilon_{0,H,V}, \quad (1)$$

where the Jones Matrix,

$$\mathcal{J}_{H,V} = \begin{pmatrix} j_{HH} & j_{HV} \\ j_{VH} & j_{VV} \end{pmatrix} \quad (2)$$

and the electric field vector,

$$\epsilon'_{H,V}(x, y, i, v) = \begin{pmatrix} E_{HH} \\ E_{VV} \end{pmatrix}. \quad (3)$$

We assume here that for narrow channel widths, the electromagnetic wave can be considered to be monochromatic and thus, Jones algebra is applicable. Hence, in order to get the true measurement of the electric field at the position of the FRB, one has to correct for the primary beam Jones matrix. In order to obtain $\mathcal{J}_{H,V}$, we used the measurements from de Villiers (2023) obtained from holography experiments with the MeerKAT telescope. Assuming that the Jones matrix for the primary beam does not change significantly with elevation, we use equation (3) to obtain the calibrated electric field for both hands of polarization. The resulting voltages are fully calibrated and can be directly used to measure the polarization of the detected FRBs. We do note that this is not the most accurate method of calibrating the data as there is no measurement of the Jones matrix at

the location of the FRB at the time of the FRB. We caution the reader that the correction may not entirely account for the leakage and we absorb these uncertainties with an additional 5 per cent uncertainty on the estimated polarization fraction.

3 RESULTS

3.1 FRB 20220717A

FRB 20220717A was discovered during commensal observations with the MeerTime project (Bailes et al. 2020) at a DM of 637 pc cm⁻³. It was discovered at the UHF band (816 MHz) and shows clear evidence of scattering (see left panel of Fig. 3). The burst is broadband across the entire 544 MHz of bandwidth with no visible structure seen at smaller time-scales. The burst shows a low linear polarization fraction (30 ± 2 per cent) that maximizes at a rotation measure of 385.7 ± 0.4 rad m⁻². From the calibrated transient buffer data, we were able to localize the FRB to RA (J2000): $+19:33:13.0 \pm 0.9$ arcsec and Dec. (J2000): $-19:17:15.8 \pm 0.9$ arcsec after performing an astrometric correction using the sources detailed in Table A1 (left panel of Fig. 4). The errors on the position were obtained from summing in quadrature the PYBDSFerror of the source position (0.4 arcsec RA, 0.4 arcsec Dec.) and the error from the astrometric correction (0.9 arcsec).

Table 1. Various observed and measured properties of FRB 20220717A and FRB 20220905A.

FRB parameter	Unit	FRB 20220717A	FRB 20220905A
MJD		59777.8221507637	59827.7480359790
UTC		2022-07-17T19:43:53.826	2022-09-05T17:57:10.309
RA (J2000)	(hms)	19:33:13.0±0.9 arcsec	16:54:19.8±0.7 arcsec
Dec (J2000)	(dms)	-19:17:15.8±0.9 arcsec	-20:04:16.9±0.7 arcsec
l	(deg)	19.83515767	0.78476176
b	(deg)	-17.63203224	14.61426288
Detection frequency	(MHz)	816	1284
S/N-maximizing DM	(pc cm ⁻³)	637.34 ± 3.52	800.61 ± 0.60
Scattering-corrected DM	(pc cm ⁻³)	634.69 ± 0.10	-
Detection S/N		15.3	14.4
Beamformed S/N		101.1	141.9
τ_s 1 GHz	(ms)	8.2 ± 0.3	-
Scattering index		-3.7 ± 0.2	-
W_{50p}^a	(ms)	8.4 ± 0.3	1.1 ± 0.1
W_{10p}^a	(ms)	20.1 ± 0.6	-
W_{eq}^a	(ms)	10.0 ± 0.3	-
RM	(rad m ⁻²)	385.7 ± 0.4	-83.1 ± 1.9
S_{peak}	(Jy)	0.34 ± 0.03	6.40 ± 0.04
F	(Jy ms)	6.83 ± 0.03	7.0 ± 0.6
DM _{NE2001}	(pc cm ⁻³)	118	154
DM _{YMW16}	(pc cm ⁻³)	83	104
DM _{halo}	(pc cm ⁻³)	86	115

^aMeasured at 1020.3 MHz.

3.2 FRB 20220905A

FRB 20220905A was discovered during a MeerTime (Bailes et al. 2020) observation at UTC 17:01:04. The FRB was detected at L band (1284 MHz) in the incoherent beam which triggered the storage of complex voltage data in the transient buffer. The FRB was detected at a DM of 800.6 pc cm⁻³ and shows no evidence of scattering or any emission at shorter time-scales (see right panel of Fig. 3). Similar to FRB 20220717A, the FRB shows a low degree of linear polarization at a rotation measure of -83.81 ± 1.9 rad m⁻². The FRB was localized to RA (J2000): 16:54:19.8±0.7 arcsec and Dec. (J2000): -20:04:16.9±0.7 arcsec (right panel of Fig. 4) which led to the immediate optical follow-up and identifying the host galaxy as shown below. The coordinates were obtained after performing an astrometric correction with the sources listed in Table 1. The errors on the position were obtained from summing in quadrature the PYBDSF error of the source position (0.09 arcsec in RA, 0.2 arcsec in Dec.) and the error from the astrometric correction (0.7 arcsec). The astrometric corrections are detailed in the Appendix.

3.3 Optical observations

We obtained deep imaging of the field of FRB 20220905A with the Gemini Multi-Object Spectrograph on the 8-m Gemini South Telescope (Gimeno et al. 2016) to identify all possible host candidates (Program GS-2022B-Q-123, PI Gordon). We obtained 20x120s in r -band on 11 October 2022 UTC and 25 x 100 s in z -band on 12 October 2022 UTC. Both data sets were reduced using the POTPyRI⁹ pipeline. Then, we utilized the Probabilistic Association of Transients to its Host (PATH) method to link the transient to a host galaxy, as outlined in Aggarwal et al. (2021). We used photutils to perform photometry and found 15 candidates within 30 arcsec of the FRB localization (see Fig. 5). The prior that the host is unseen was set to

be $P(U) = 0.05$, and the offset prior was set to 50 per cent of the half-light radius of the host. PATH output indicated that the host is unseen (see Table A3). The PATH unseen posterior $P(U|x) \sim 1$. We also conducted a manual inspection of the image, during which we noted a faint $\approx 3\sigma$ source offset 0.9 arcsec from the FRB-localization and with an angular size of 1.1 arcsec. If we include this source in the list of candidates, it is assigned a very high PATH posterior ($P(O|x) \approx 0.98$). However, this candidate is still a tentative source.

The FRB 20220717A localization is close (0.6 arcsec) to a galaxy seen in PanSTARRS DR1 archival data of the field (see Fig. 5). A PATH analysis on the image confirmed the source (PSO J293.3038-19.2876) as the host galaxy of FRB 20220717A with a high posterior probability ($P(O|x) \approx 0.97$) as shown in Table A4. We obtained spectroscopy of the host of FRB 20220717A on 28 October 2022 UTC with the Goodman High Throughput Spectrograph on the 4-m Southern Astrophysical Research Telescope (SOAR; Clemens, Crain & Anderson 2004) to determine its redshift, totalling 2 × 1200 s of science exposure (Program SOAR2022-007B, PI Gordon). We used the M1 400 lines/mm grating covering a wavelength range of 3000–7050 Å in conjunction with the BlueCam and a 1.0 arcsec slit. The position angle was oriented to align the host with a nearby object for ease of identification during reduction. The data were processed with PYPEIT (Prochaska et al. 2020), using a quicklook reduction to identify the host redshift.

We obtained a second spectrum of the host of FRB 20220717A with Keck/DEIMOS on 27 October 2022 UTC by taking a single 900s exposure (Program U129, PI Prochaska). We used the ZD 600 lines/mm grating for a wavelength coverage of 4550–9450 Å with a 1.0 arcsec slit. The data were reduced fully using the PyPEIT reduction package (Prochaska et al. 2020) to produce a flux-calibrated 1D spectrum of the host galaxy. This spectrum shows substantial contamination from skylines, likely due to a manufacturing issue during production of the relevant slit mask, which we were unable to remove fully in the reduction process. None the less, we perform all further analysis on this DEIMOS spectrum. These observations yield

⁹<https://github.com/CIERA-Transients/POTPyRI>

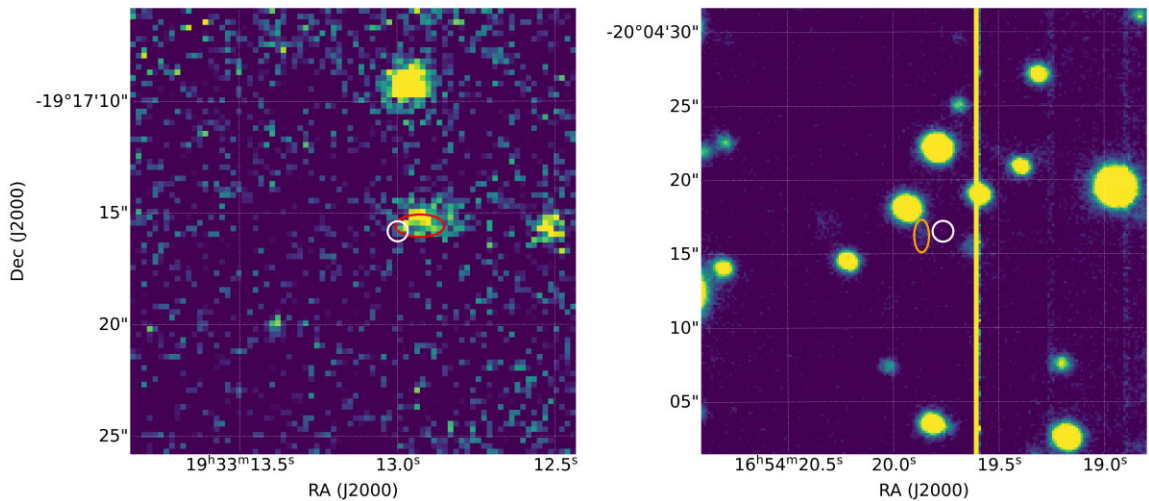


Figure 5. Left: Archival PanSTARRS DR1 image of the field surrounding the FRB20220717A localization (see PATH results in Table A4). The best known 1σ position of the FRB is shown by the white ellipse and the red ellipse shows the host galaxy. Right: GMOS image showing FRB20220905A localization field crowded with stars (PATH results in Table A3), white ellipse is 1σ localization region, orange ellipse is the tentative host for FRB20220905A.

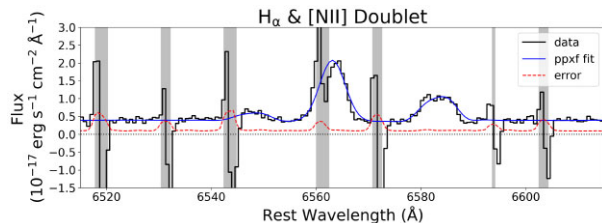


Figure 6. Keck/DEIMOS spectrum of the FRB20220717A host galaxy showing the $\text{H}\alpha$ emission line at 6563 Å and neighbouring $[\text{N II}]$ emission at 6548 Å and 6584 Å at a common redshift $z = 0.3633$. The black histogram shows the spectral data, while the observed error is shown in red. Blue shows the PPXF model fit to the data. Grey vertical regions indicate sky lines that are masked in the spectral fitting process.

a spectroscopic redshift of $z = 0.36295 \pm 0.00018$ for the FRB host galaxy.

In order to confirm the redshift and to measure $\text{H}\alpha$ emission, the DEIMOS spectrum was fit using the PPXF spectral fitting package to fit both the spectral continuum and emission features (Cappellari 2023). Due to the presence of poorly subtracted sky lines in the spectrum, we masked these regions out of the PPXF fit. Masking was applied to any region with a flux measurement error above $0.25 \times 10^{-17} \text{ erg s}^{-1} \text{ cm}^{-2} \text{ Å}^{-1}$, as well as any region with a flux measurement $< 0.2 \times 10^{-17} \text{ erg s}^{-1} \text{ cm}^{-2} \text{ Å}^{-1}$ as this is indicative of oversubtraction. The resulting PPXF fit to the $\text{H}\alpha$ feature is shown in Fig. 6. Integrating this fit yields an $\text{H}\alpha$ flux of $17.08 \pm 3.7 \times 10^{-17} \text{ erg s}^{-1} \text{ cm}^{-2}$, uncorrected for Galactic extinction.

Using the linear model to compute star formation rate (SFR) from $\text{H}\alpha$ emission given in Kennicutt, Tamblyn & Congdon (1994), this galaxy is observed to have an SFR of $0.65 \pm 0.14 \text{ M}_\odot \text{ yr}^{-1}$. Unfortunately this emission feature falls directly on an observed sky line, which was masked out of the flux integration measurements. Though we fit this feature using a Gaussian profile, the nearby $[\text{N II}]\lambda 6584$ line shows a double-peaked profile indicating rotational broadening of the emission features. The limited data quality likely makes our measurement on $\text{H}\alpha$ an underestimation, and therefore

our result for SFR computed therefrom should also be understood as a lower limit.

We estimate the host galaxy DM contribution using the $\text{H}\alpha$ emission measure (EM) as described in Tendulkar et al. (2017):

$$\text{DM}_{\text{host}} = 387 \text{ pc cm}^{-3} L_{\text{kpc}}^{1/2} \left[\frac{4f_f}{\zeta(1+\epsilon^2)} \right]^{1/2} \left(\frac{\text{EM}}{600 \text{ pc cm}^{-6}} \right)^{1/2}, \quad (4)$$

where f_f is the volume filling factor of the ionized clouds, $\zeta \geq 1$ specifies cloud-to-cloud density variations, $\epsilon \leq 1$ is the fractional variation within discrete clouds, and L_{kpc} is the depth of the total ionized region in kpc. As in Tendulkar et al. (2017), we assume that $\zeta = 2$ (indicating 100 per cent variation between clouds) and that $\epsilon = 1$ (indicating that the electron density within clouds is fully modulated). We also assume that $f_f = 1$.

We compute EM from the observed $\text{H}\alpha$ surface brightness as described in Reynolds (1977). Because the PanSTARRS image of this host cannot be used to constrain its morphology, we cannot place good constraints on L_{kpc} . If we take L_{kpc} to be 0.150, the expected value for a Milky Way-like spiral galaxy with the FRB in its mid-plane, we can thus estimate a DM_{host} contribution of $\sim 100 \text{ pc cm}^{-3}$ (Kalberla & Kerp 2009).

4 DISCUSSION

4.1 Benefits of complex voltage capture

The ability to save complex voltage data from each antenna at the native time resolution allows MeerTRAP to overcome these limitations of post-detection analysis. Along with the ability to localize the FRBs by creating images from these data, we can also study FRBs at the finest possible time-resolution and also obtain polarization information. We also note that the ability to beamform the transient buffer data to the correct location of the FRB also enables one to increase the sensitivity of the telescope towards these FRBs significantly since the transient buffer data includes all the telescopes that were used in the observations as opposed to the limit of 40 dishes that is used in the real-time coherent searches for MeerTRAP.

Furthermore, it also accounts for the reduction in S/N in the search due to offset of the FRB from the boresight of the coherent beam in which it was discovered. This is clearly shown by the difference in the estimated S/N of the bursts in the real-time search and the processed transient buffer data in Table 1. This ability enables one to reveal fainter features in the emission across the dynamic spectrum that may be washed out in the down-sampled data. The results presented in this paper reiterate the power of saving complex voltage data for FRBs.

4.2 Complex environments around FRB progenitors

Both the FRBs presented here show flat polarization position angles (PAs). This is consistent with PAs observed for most one-off FRBs (Pandhi et al. 2024). It is important to note that PAs are also flattened due to scattering in the intervening medium based on observations of Galactic pulsars (Li & Han 2003; Karastergiou 2009). FRB 20220717A and FRB 20220905A show a very low degree of linear polarization (10 ± 2 per cent and 17.5 ± 1.5 per cent) which is consistent with what has been recently seen for one-off FRBs (Pandhi et al. 2024; Sherman et al. 2024). One of the possibilities of depolarization could be instrumental but any residual phase and gain differential between the two dipoles of the receiver will only increase the linear/circular polarization fraction hence depolarization is unlikely to be due to calibration inaccuracies. The calibration and leakage correction for circular polarization measurements with MeerKAT is not yet well understood. As such, we could not reliably measure the circular polarization of these FRBs.

Recent studies of linear polarization of a large sample of FRBs (Pandhi et al. 2024; Sherman et al. 2024) have shown that one-off FRBs seem to have a large diversity in the degree of linear polarization. On the other hand, linear polarization fractions with values ranging between 90 and 100 percent (McKinven et al. 2023) seems to be a distinct property of the repeating FRBs. These observations suggest a possible dichotomy in the nature of FRB progenitors, a key open question in the field. One argument for a small degree of linear polarization for some of the one-off FRBs could be a complex environment in the vicinity of the FRB source causing depolarization of radiation due to RM scattering (Plavin et al. 2022; Beniamini et al. 2022). Such environments could explain the large contribution by the host to the total DM in a number of apparently one-off FRBs recently discovered by ASKAP and MeerKAT (Caleb et al. 2019; Bhandari et al. 2023). This might be true for FRB 20220717A with a potentially significant RM in the source frame but this conjecture is hard to reconcile with FRB 20220905A. To investigate the source of RM contribution, we compute the expected Galactic contribution to the RM along the line of sights of the two FRBs presented in this paper. To do this we use the Galactic RM maps created by Hutschenreuter et al. (2022) to obtain the mean RM contribution by the Galaxy. The Galactic contribution along the line of sight to FRB 20220905A and FRB 20220717A is small (45 ± 17 and 0 ± 24 rad m $^{-2}$), suggesting that the majority of the RM can be attributed to the host galaxy and any foreground, magnetized plasma.

4.3 Origin of scattering in FRB 20220717A

The burst from FRB 20220717A exhibits a strong scattering feature. In order to characterize it, we fit the profile with a combination of a Gaussian and a scattering function of the intervening medium. The scattering function can be approximated by an exponential quantified by the scattering time-scale τ . We use the SCATFIT software

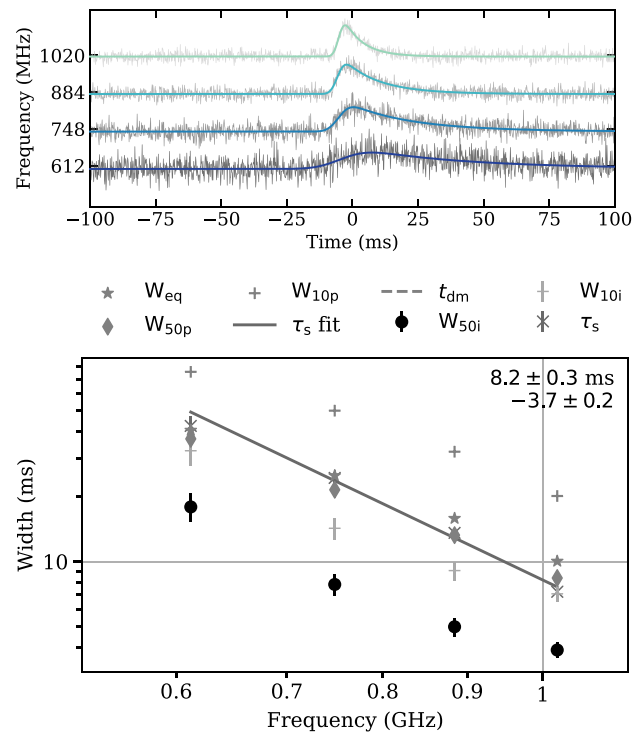


Figure 7. Top panel: Scattered profile of FRB 20220717A shown in 4 subbands with the corresponding best-fitting model. Bottom panel: Estimate of scattering timescale and pulse width as a function of frequency along with the best-fitting linear fit. The two numbers at the top right show the scattering time-scale at 1 GHz and scaling index of scattering.

(Jankowski 2022; Jankowski et al. 2023) to fit the scattering function as a function of frequency. We split the data into four subbands such that there was enough signal in each to obtain a robust fit to the burst profile. Fig. 7 shows the results of our analysis. We obtain $\tau = 8.2 \pm 0.3$ ms at 1 GHz with the scattering time-scale scaling with frequency as a power law with an exponent, $\alpha = -3.7 \pm 0.2$. The analysis also optimizes for the DM while fitting the scattering function so as to maximize the S/N which gives us the best-fitting DM of 634.69 pc cm $^{-3}$.

The total DM of any FRB is made of different components such that,

$$\begin{aligned} \text{DM}_{\text{obs}} &= \text{DM}_{\text{ISM}} + \text{DM}_{\text{halo}} + \text{DM}_{\text{EG}}, \\ \text{DM}_{\text{EG}} &= \text{DM}_{\text{cosmic}} + \frac{\text{DM}_{\text{host}}}{1+z}, \end{aligned} \quad (5)$$

where DM_{ISM} is the contribution from the MW's ISM and DM_{halo} is the contribution from the MW halo. DM_{EG} is the extragalactic DM contribution composed of $\text{DM}_{\text{cosmic}}$ which is the contribution from the cosmic web (combined effects of the intergalactic medium (IGM) and intervening galaxies), and $\frac{\text{DM}_{\text{host}}}{1+z}$ which is the redshifted contribution from the host galaxy's ISM including its halo and any gas in the immediate vicinity of the FRB source. An FRB with a known redshift allows us to estimate $\text{DM}_{\text{cosmic}}$ and given that we can estimate DM_{ISM} and DM_{halo} , we can then infer an estimate for $\frac{\text{DM}_{\text{host}}}{1+z}$. An increasing sample of accurately localized FRBs with identified host galaxies gives us an opportunity to assess the component of DM that contributes most significantly to the observed scattering in them.

To do this, we collated all the well localized, scattered FRBs from ASKAP and MeerTRAP with measured redshifts (Driessen et al.

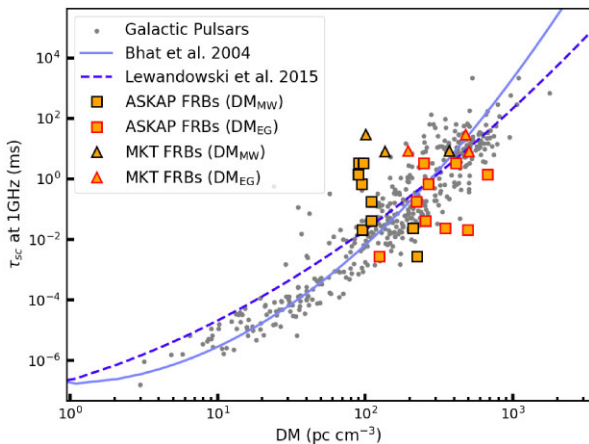


Figure 8. Dispersion measure versus scattering timescale at 1 GHz. The grey points show the measurement for Galactic pulsars. The squares and triangles show scattering time-scale as a function of different DM components for all ASKAP and MeerTRAP localized FRBs. Here, DM_{MW} refers to the DM contribution from the ISM of the Milky Way. Here, we assume the MW halo contribution of 52.8 pc cm^{-3} (Cook et al. 2023).

2022; James et al. 2022; Baptista et al. 2023; Caleb et al. 2023) and where the DM contribution from the host can be estimated based on the method presented in (James et al. 2022). Then we looked for any correlations between the scattering timescale at 1 GHz and the DM contributions due to different components as shown in Fig. 8. For majority of the FRBs, the expected scattering from the Milky Way for these FRBs is a lot smaller compared to the measured scattering timescale. It potentially hints at the fact that the measured scattering for FRBs cannot be explained by the ISM in our own Galaxy. Therefore, the scattering should be dominated by turbulence in the foreground galaxies and/or the host galaxy itself. For the published MeerKAT FRBs, it is evident that DM_{host} can account for most of the scattering observed, further validating the claim made in Chawla et al. (2022).

4.4 Host Galaxy contribution to the DM of FRB 20220717A

As discussed in the previous section, the dispersion of FRBs makes them excellent probes for unraveling the structure of the cosmic web. This was initially shown by Macquart et al. (2020) who provided a relationship between the expected DM_{EG} and the redshift of the FRB host (assuming a typical DM_{host} of 100 units). FRB 20220717A shows a host DM contribution that is consistent with these predictions. We compute the expected DM_{cosmic} for FRB 20220717A using the Macquart relation with the same assumptions as presented in Caleb et al. (2023). Assuming a DM_{host} of 100 pc cm^{-3} and a MW ISM and halo contribution of 83 pc cm^{-3} (from the YMW16 model) and 52 pc cm^{-3} using the model from Cook et al. (2023), we obtain DM_{cosmic} of $\simeq 402 \text{ pc cm}^{-3}$. This DM contribution from the IGM is within the scatter of the Macquart relation. It is worth noting that if we assume that the RM is mostly dominated by the host galaxy, the expected RM in the reference frame of the host, $RM_{hostframe} = RM(1+z)^2 \simeq 720 \text{ rad m}^{-2}$. This is a large value of RM that is typically measured in the dense star-forming regions of a Galaxy (Van Eck et al. 2021). Furthermore, the high star-formation rate measured for the host galaxy can explain the turbulent and dense regions in the galaxy. These diagnostic measurements along with a large $H\alpha$ flux from the host galaxy spectrum

suggests that FRB 20220717A may lie in a dense region of its host galaxy.

5 CONCLUSIONS

In summary, we present the discovery and the subsequent subarcsecond localization of two FRBs with the MeerTRAP instrument. The transient buffer capture functionality has allowed us to localize and identify the host galaxies and study the polarization of these bursts. Both FRB 20220717A and FRB 20220905A show a low degree of linear polarization with no conclusive evidence on the presence or absence of circular polarization due to calibration issues. This is consistent with what is observed for one-off FRBs and may hint at the fact that linear polarization fraction could be a distinguishing property between the apparently repeating and non-repeating population of FRBs. It also suggests that there is a distribution in the polarization fraction in FRBs akin to single pulses seen from neutron stars and could be attributed to depolarization near the source. The host DM contribution for FRB 20220717A is estimated to be around 100 pc cm^{-3} which is consistent with the measured $H\alpha$ flux. The high star-formation rate of the host galaxy and the RM measurement suggests that the FRB may lie within a dense region of the galaxy. FRB 20220717A also exhibits scattering which can be mostly attributed to the host galaxy and the intervening medium, consistent with scattering seen in the FRB population. The transient buffer mode is fully operational on MeerTRAP with transient buffer data on more than 20 FRBs that are currently being investigated. This study again demonstrates the power of saving raw voltage data for accurately localizing FRBs and further promotes the deployment of such systems on all real-time FRB detection systems around the world.

ACKNOWLEDGEMENTS

The authors would like to thank the referee for their comments that significantly improved the manuscript. The MeerKAT telescope is operated by the South African Radio Astronomy Observatory, which is a facility of the National Research Foundation, an agency of the Department of Science and Innovation (DSI). The MeerTRAP collaboration would like to thank the MeerKAT Large Survey Project teams for allowing MeerTRAP to observe commensally. The MeerTRAP collaboration acknowledges funding from the European Research Council (ERC) under the European Union's Horizon 2020 research and innovation programme (grant agreement no. 694745). The authors also acknowledge the usage of TRAPUM infrastructure funded and installed by the Max-Planck-Institut für Radioastronomie and the Max-Planck-Gesellschaft. KMR would like to thank Mattieu DeVilliers and Ludwig Schwarz for useful discussions regarding off-boresight polarization calibration for MeerKAT. The authors would like to thank the South African Radio Astronomy Observatory (SARAO) for immense support during the commissioning of the transient buffer mode. KMR acknowledges support from the Vici research programme 'ARGO' with project number 639.043.815, financed by the Dutch Research Council (NWO). AM acknowledges support from the U.S. National Science Foundation through grant AST-2206492 and from the Nantucket Maria Mitchell Association. MC acknowledges support of an Australian Research Council Discovery Early Career Research Award (project number DE220100819) funded by the Australian Government. MB acknowledges support from the Bundesministerium für Bildung und Forschung(BMBF) D-MeerkAT award 05A17VH3 (Verbundprojekt D-MeerkAT).

DATA AVAILABILITY

The processed data products from the transient buffer corresponding to FRB 20220905A and FRB 20220717A and the corresponding scripts will be made available to others upon reasonable request.

REFERENCES

Aggarwal K., Budavári T., Deller A. T., Eftekhari T., James C. W., Prochaska J. X., Tendulkar S. P., 2021, *ApJ*, 911, 95

Bailes M. et al., 2020, *PASA*, 37, e028

Bannister K. W., 2018, *Nat. Astron.*, 2, 922

Baptista J. et al., 2024, *ApJ* 965 1

Beniamini (2022) *Monthly Notices of the Royal Astronomical Society*, 4654, 0035-8711

Beroiz M., Cabral J. B., Sanchez B., 2020, *Astron. Comput.*, 32, 100384

Bhandari S. et al., 2023, *ApJ*, 948, 67

Bochenek C. D., Ravi V., Belov K. V., Hallinan G., Kocz J., Kulkarni S. R., McKenna D. L., 2020, *Nature*, 587, 59

Caleb M. et al., 2023, *MNRAS*, 524, 2064

Caleb M., Stappers B. W., Rajwade K., Flynn C., 2019, *MNRAS*, 484, 5500

Cappellari M., 2023, *MNRAS*, 526, 3273

Chawla P. et al., 2022, *ApJ*, 927, 35

Chen W., Barr E., Karuppusamy R., Kramer M., Stappers B., 2021, *J. Astron. Instr.*, 10, 2150013

CHIME/FRB Collaboration et al., 2018, *ApJ*, 863, 48

CHIME/FRB Collaboration et al., 2020, *Nature*, 587, 54

Clark M. A., La Plante P. C., Greenhill L. J., 2012, *The International Journal of High Performance Computing Applications* 27

Clemens J. C., Crain J. A., Anderson R., 2004, in Moorwood A. F. M., Iye M., eds, Proc. SPIE Conf. Ser. Vol. 5492, Ground-based Instrumentation for Astronomy. SPIE, Bellingham, p. 331

Cook A. M. et al., 2023, *ApJ*, 946, 58

de Villiers M. S., 2023, *AJ*, 165, 78

Deller A. T. et al., 2011, *PASP*, 123, 275

Deller A. T., Tingay S. J., Bailes M., West C., 2007, *PASP*, 119, 318

Driessen L. N. et al., 2022, *MNRAS*, 512, 5037

Driessen L. N. et al., 2024, *MNRAS*, 527, 3659

Duchesne S. W. et al., 2023, *Publ. Astron. Soc. Aust.*, 40, e034

Gimeno G. et al., 2016, in Evans C. J., Simard L., Takami H., eds, SPIE Conf. Ser. Vol. 9908, Ground-based and Airborne Instrumentation for Astronomy VI. SPIE, Bellingham, p. 99082S

Hale C. L. et al., 2021, *Publ. Astron. Soc. Aust.*, 38, e058

Hutschenreuter S. et al., 2022, *A&A*, 657, A43

James C. W. et al., 2022, *MNRAS*, 516, 4862

Jankowski F. et al., 2022, in Ruiz J. E., Pierfederici F., Teuben P., eds, *Astron. Soc. Pac. Conf. Ser. Vol. 532*. Astron. Soc. Pac., San Francisco, p. 273

Jankowski F. et al., 2023, *MNRAS*, 524, 4275

Jankowski F., 2022, Astrophysics Source Code Library, record ascl:2208.003

Jonas J., MeerKAT Team, 2016, in MeerKAT Science: On the Pathway to the SKA. p. 1

Kalberla P. M. W., Kerp J., 2009, *ARA&A*, 47, 27

Karastergiou A., 2009, *MNRAS*, 392, L60

Kennicutt Robert C. J., Tamblyn P., Congdon C. E., 1994, *ApJ*, 435, 22

Kirsten F. et al., 2022, *Nature*, 602, 585

Li X. H., Han J. L., 2003, *A&A*, 410, 253

Lorimer D. R., Bailes M., McLaughlin M. A., Narkevic D. J., Crawford F., 2007, *Science*, 318, 777

Macquart J. P. et al., 2020, *Nature*, 581, 391

McConnell D., Sadler E. M., Murphy T., Ekers R. D., 2012, *MNRAS*, 422, 1527

Mckinven R. et al., 2023, *ApJ*, 951, 82

McMullin J. P., Waters B., Schiebel D., Young W., Golap K., 2007, in Shaw R. A., Hill F., Bell D. J., eds, ASP Conf. Ser. Vol. 376, Astronomical Data Analysis Software and Systems XVI. Astron. Soc. Pac., San Francisco, p. 127

Pandhi A. et al., 2024, *ApJ*, 968, 2

Petroff E. et al., 2017, preprint ([arXiv:1710.08155](https://arxiv.org/abs/1710.08155))

Petrov L., Phillips C., Bertarini A., Murphy T., Sadler E. M., 2011, *MNRAS*, 414, 2528

Plavin A., Paragi Z., Marcote B., Keimpema A., Hessels J. W. T., Nimmo K., Vedantham H. K., Spitler L. G., 2022, *MNRAS*, 511, 6033

Prochaska J. et al., 2020, *J. Open Source Softw.*, 5, 2308

Rajwade K. et al., 2020, in Evans C. J., Bryant J. J., Motohara K. eds, Proc. SPIE Conf. Ser. Vol. 11447, Ground-based and Airborne Instrumentation for Astronomy VIII. SPIE, Bellingham, p. 114470J

Rajwade K. M. et al., 2022, *MNRAS*, 514, 1961

Ravi V. et al., 2023, *ApJ*, 949, L3

Reynolds R. J., 1977, *ApJ*, 216, 433

Seaman R. et al., 2011, *International Virtual Observatory Alliance* Preprint ([arXiv:1110.0523](https://arxiv.org/abs/1110.0523)),

Sherman M. B. et al., 2024, *ApJ*, 964, 131

Swinbank J., 2014, *Astron. Comput.*, 7–8, 12

Tendulkar S. P. et al., 2017, *ApJ*, 834, L7

The CASA Team et al., 2022, *PASP*, 134, 114501

van der Byl A. et al., 2022, *J. Astron. Telesc. Instrum. Syst.*, 8, 011006

Van Eck C. L. et al., 2021, *ApJS*, 253, 48

APPENDIX: ASTROMETRY SOURCES

Tables A1 and A2 detail the sources that were used to perform the astrometric correction for FRB 20220710A and FRB 20220905A, respectively. In both cases, no LCS1 or ATPMN sources were available, but several RFC sources laid in a 3.5° radius from the images phase centre. We thus used the RFC sources to align the positions of the matching RACS sources, and thus obtained

Table A1. Sources used for the astrometric correction of FRB 20220717A. The first group were the RFC sources used to align RACS, while the second group are the corrected RACS sources used to align the MeerTRAP sources.

RFC source	RACS source	Sep. before (")	Sep. after (")
J1924-1949	J192441.4-194949	1.35	0.13
J1925-1813	J192512.4-181303	1.44	0.36
J1928-2035	J192809.1-203543	1.18	0.32
J1928-1707	J192851.2-170758	1.71	0.20
J1930-2053	J193010.3-205304	1.25	0.18
J1931-2025	J193149.0-202537	1.11	0.19
J1935-1804	J193509.3-180444	1.53	0.02
Mean		1.36	0.20
RACS Source		Sep. before (")	Sep. after (")
J192139.2-175408		1.75	1.23
J192113.6-174846		1.60	0.98
J192109.9-170507		1.54	1.57
J192047.2-174602		1.26	0.60
J192045.1-164410		0.84	0.47
J192043.7-202838		1.91	0.83
J192043.6-185557		0.77	0.36
J192036.7-172940		2.28	0.87
J192036.5-202954		1.29	0.78
J192030.7-170746		0.80	0.26
J192032.7-191010		0.50	0.11
J192029.1-163509		1.79	1.01
J192017.5-174030		1.10	0.78
J192017.1-195115		1.03	0.63
J192008.7-203228		1.60	0.67
J192015.6-181904		3.29	0.86
J191941.1-180128		2.06	1.81
J191937.9-195826		1.80	0.86
J191919.7-205020		1.82	1.05
Mean		1.53	0.83

Table A2. Sources used for the astrometric correction of FRB 20220905A. The first group were the RFC sources used to align RACS, while the second group are the corrected RACS sources used to align the MeerTRAP sources.

RFC source	RACS source	Sep. before (")	Sep. after (")
J1644-2156	J164443.3-215608	1.15	0.03
J1647-1926	J164753.7-192618	0.65	0.24
J1650-2010	J165010.5-201012	0.93	0.24
J1656-2010	J165655.1-201056	0.55	0.13
J1657-2004	J165733.2-200434	0.88	0.25
J1701-2007	J170135.4-200759	0.63	0.29
J1703-2110	J170327.4-211049	0.70	0.22
	Mean	0.79	0.20
RACS source		Sep. before (")	Sep. after (")
J165532.6-184546		2.45	0.33
J165204.9-212536		1.29	0.08
J165128.6-221213		0.99	0.49
J165118.8-231359		1.36	0.24
J165115.5-195629		1.30	0.12
J165059.1-230533		1.40	0.67
J165056.1-211911		0.28	0.58
J165054.4-232933		1.65	1.93
J165037.4-222326		1.26	0.57
J165033.9-201748		0.85	0.49
J164954.1-214558		0.07	0.26
J164953.0-220609		1.13	0.90
J164939.7-201149		1.01	0.85
J164910.4-183237		0.39	1.29
J164852.8-225423		2.11	2.19
J164846.4-214847		0.55	0.23
J164813.4-215206		1.74	0.83
J164753.7-192618		0.87	0.21
J164638.1-210942		1.64	0.11
J164528.9-195622		2.16	0.44
J164508.8-224833		1.40	0.89
J164438.8-184024		2.06	0.21
	Mean	1.27	0.63

Table A3. PATH analysis results for FRB 20220905A showing the top 5 most probable host galaxy candidate. Here $P(O|x)$ denotes the posterior probability of a galaxy being the host for the FRB. Most of the candidates have insignificant PATH posteriors. The value of 10^{-6} roughly corresponds to 0.001 per cent interval for a Gaussian probability density function.

RA J2000	Dec. J2000	Ang-size (arcsec)	Mag (arcsec)	Sep	$P(O x)$
16:54:20.31	-20:04:17.13	0.2	24.4	7.3	$\ll 10^{-6}$
16:54:19.81	-20:04:03.52	0.3	21.1	12.7	$\ll 10^{-6}$
16:54:20.02	-20:04:07.41	0.2	23.6	9.4	$\ll 10^{-6}$
16:54:19.20	-20:04:07.62	0.2	22.7	12.0	$\ll 10^{-6}$
16:54:19.30	-20:04:27.19	0.2	21.8	13.0	$\ll 10^{-6}$

Table A4. PATH analysis results for FRB 20220717A showing the most probable host galaxy candidates.

RA J2000	Dec. J2000	Ang-size (arcsec)	Mag (arcsec)	Sep	$P(O x)$
19:33:12.91	-19:17:15.42	2.2	21.8	0.6	9.69×10^{-1}
19:33:13.12	-19:17:09.35	2.2	20.9	5.6	2.28×10^{-2}
19:33:12.53	-19:17:15.74	2.2	22.6	5.3	5.86×10^{-3}
19:33:13.17	-19:17:30.54	2.2	24.9	16.2	7.37×10^{-58}

the transformation to correct the RACS source position. Next we used the RACS sources matching the MeerTRAP sources obtained with PYBDSF to perform the final astrometric transformation. The resulting mean offsets between RFC and RACS, and RACS and MeerTRAP after each transformation, were added in quadrature to obtain the astrometric uncertainty. For FRB 20220717A, this is $\Delta\theta = (0.20^2 + 0.83^2)^{1/2} = 0.85''$, while for FRB 20220905A, we get $\Delta\theta = (0.20^2 + 0.63^2)^{1/2} = 0.66''$.

This paper has been typeset from a $\text{\TeX}/\text{\LaTeX}$ file prepared by the author.